

The interplay of field-tunable strongly correlated states in a multi-orbital moiré system

Aidan J. Campbell,¹ Valerio Vitale,^{2,3} Mauro Brotons-Gisbert,¹ Hyeonjun Baek,¹
Takashi Taniguchi,⁴ Kenji Watanabe,⁵ Johannes Lischner,³ and Brian D. Gerardot^{1,*}

¹*Institute of Photonics and Quantum Sciences, SUPA, Heriot-Watt University, Edinburgh EH14 4AS, UK*

²*Dipartimento di Fisica, Università di Trieste, strada Costiera 11, 34151, Trieste, Italy*

³*Departments of Materials and Physics and the Thomas Young Centre for Theory and Simulation of Materials, Imperial College London, South Kensington Campus, London SW7 2AZ, United Kingdom*

⁴*International Center for Materials Nanoarchitectonics, National*

Institute for Materials Science, 1-1 Namiki, Tsukuba 305-0044, Japan

⁵*Research Center for Functional Materials, National Institute for Materials Science, 1-1 Namiki, Tsukuba 305-0044, Japan*

(Dated: March 10, 2023)

The interplay of charge, spin, lattice, and orbital degrees of freedom leads to a wide range of emergent phenomena in strongly correlated systems. In heterobilayer transition metal dichalcogenide moiré systems, recent observations of Mott insulators and generalized Wigner crystals are well described by triangular lattice single-orbital Hubbard models based on K-valley derived moiré bands. Richer phase diagrams, mapped onto multi-orbital Hubbard models, are possible with hexagonal lattices in Γ -valley derived moiré bands and additional layer degrees of freedom. Here we report the tunable interaction between strongly correlated hole states hosted by Γ - and K-derived moiré bands in a monolayer MoSe₂ / natural WSe₂ bilayer device. To precisely probe the nature of the correlated states, we optically characterise the behaviour of exciton-polarons and distinguish the layer and valley degrees of freedom. We find that the honeycomb Γ -band gives rise to a charge-transfer insulator described by a two-orbital Hubbard model with inequivalent Γ_A and Γ_B orbitals. With an out-of-plane electric field, we re-order the Γ_B - and K-derived bands energetically, driving an abrupt redistribution of carriers to the layer-polarized K orbital where new correlated states are observed. Finally, by fine-tuning the band-alignment, we obtain degeneracy of the Γ_B and K orbitals at the Fermi level. In this critical condition, stable Wigner crystals with carriers distributed across the two orbitals are observed until the Fermi-level reaches one hole per lattice site, whereupon the system collapses into a filled Γ_B orbital. Our results establish a platform to investigate the interplay of charge, spin, lattice, and layer geometry in multi-orbital Hubbard model Hamiltonians.

INTRODUCTION

Although conceptually simple, the single-orbital two-dimensional Hubbard model can describe many ingredients of strongly correlated systems. However, real quantum materials are typically described using multi-orbital Hubbard models. For instance, doping in the two-orbital charge-transfer insulator has been connected to high-temperature superconductivity in the cuprates [1–3] and iron-based superconductors demand Hubbard models that account for multiple orbitals degenerate at the Fermi level [4]. While significant challenges exist to accurately solve the single-orbital Hubbard model and its derivatives, the phase diagrams of more complex multi-orbital models become even more intractable to elucidate; they sensitively depend on the interplay of the different degrees of freedom [5]. Hence, there is a strong motivation to develop platforms for strongly correlated physics which are relatively simple yet possess a high degree of tunability such that the emergent physics can be probed and accurately mapped onto paradigmatic quantum Hamiltonians [6, 7].

Synthetic moiré superlattices, formed by stacking two atomic layers with a lattice mismatch and / or relative twist angle, have emerged as a versatile solid-state plat-

form that potentially fulfils these criteria [7–9]. The versatility of moiré materials arises from the impressive array of tuning knobs that can effectively control the moiré lattice and adjust the strength and nature of the particle interactions. For instance, electrostatic gating can fine-tune the fractional filling (ν) of the lattice with carriers (electrons or holes, ν_e or ν_h , respectively), displacement fields can adjust the moiré potential depth [10, 11], and the long-range Coulomb interactions can be manipulated with screening gates [12, 13]. Further, in semiconducting transition metal dichalcogenide (TMD) moiré systems, the Coulomb interaction strengths between particles in the moiré lattice can be continuously tuned via the moiré period [14, 15]. Additionally, different real-space lattice geometries can be found in the low energy valence moiré bands, dependent on the valley degree of freedom: moiré orbitals on a triangular lattice are generally found for K-valley moiré bands localized on a single atomic layer [14–21] while honeycomb lattices are found for Γ -valley moiré bands spread across each layer [22–28]. Notably, the energetic ordering of Γ - versus K-derived valence moiré bands is sensitively dependent on material combination, twist angle, and atomic relaxation effects [29]. To date, most experimental observations of correlated states in both TMD moiré homo- and hetero-bilayers have been suffi-

ciently described by single-band Hubbard models. Thus, experimentally realizing tunable moiré systems that portray multi-orbital Hubbard physics remains an exciting opportunity in this emerging platform.

Here, by adding a non-twisted monolayer to a moiré hetero-bilayer (HBL) device to create a hetero-trilayer (HTL) device with only one moiré interface, we demonstrate a new degree of freedom to realize an extended t - U - \mathcal{V} three-orbital Hubbard system based on low energy moiré bands at Γ and K which host distinct real-space lattice geometries. Crucially, the relative ordering of these bands can be fine-tuned with an external electric (displacement) field \vec{E} and we are able to investigate the interplay of correlated states between different orbitals. To precisely probe the nature of the correlated states, we develop an optical spectroscopy technique based on the distinctive behaviour of exciton-polarons [30–32] that unambiguously distinguishes the layer and valley degrees of freedom (see Methods).

LAYER AND VALLEY DEGREES OF FREEDOM FOR HOLES IN MOIRÉ BANDS

Our HTL sample is a natural bilayer (2L) $2H$ - WSe_2 / monolayer (1L) $MoSe_2$ device with a moiré interface period of ≈ 7 nm due to a relative twist of $\theta \approx 2.7^\circ$. Compared to a 1L WSe_2 / 1L $MoSe_2$ HBL device, the HTL provides an additional layer degree of freedom [18, 21, 33] while also raising the prospect for exploitation of the valley degree of freedom in the valence band [34]. To aid unambiguous identification of the spectral features in the HTL device, we investigate a sample (see Fig. 1d for a cross-section schematic of the device) with adjacent HBL and HTL regions with nominally identical moiré period at each WSe_2 / $MoSe_2$ interface (see Methods). Hence, the HBL serves as a reference with well understood exciton-polaron behavior in the presence of strongly correlated states [20].

Figure 1a,b shows doping (V_g)-dependent sweeps (see Methods) while monitoring the derivative of the reflection contrast with respect to energy ($d(\Delta R/R_0)/dE$) in representative HBL and HTL regions of the device, respectively, at a temperature of 4K. We observe two unequivocal signatures of the effect of the moiré potential in both regions. First, at charge neutrality, we observe two $MoSe_2$ excitonic features, labelled $MX_{Mo,1}$ and $MX_{Mo,2}$, which we assign to be $MoSe_2$ moiré intralayer excitons, in agreement with recent reports [20, 35, 36]. Second, we observe doping-dependent periodic modulations in the peak position, intensity, and linewidth of all intralayer excitonic features at V_g values corresponding to integer fractional fillings of the moiré superlattice (white dashed lines in Fig. 1a,b), indicating the formation of correlated electron and hole states. In the HTL, the V_g required to fill the moiré lattice with either one electron or one hole

per site is similar to the HBL and corresponds to a twist angle of 2.7° (see Methods).

In contrast to the HBL region, in the HTL we observe two WSe_2 intralayer exciton peaks with different transition energies due to their different dielectric environments (see sketch in Fig. 1d). The lower energy feature, labelled $X_{W,L1}^0$, is the WSe_2 neutral exciton localised in the heterostructure interface layer (L1), while the higher energy exciton, $X_{W,L2}^0$, is localised in the other layer (L2) (see Methods). This spectroscopic signature provides a clear probe to determine which WSe_2 layer is occupied by the Fermi sea under doping (via the formation of attractive exciton-polarons for each intralayer exciton). We measure multiple spatial locations in the HTL region and find the behaviour shown in the main text is general (see Suppl. Fig. S1 and Suppl. Tab. S1).

Figure 1c,e shows the valence band schematics in the moiré Brillouin zone for the HBL and HTL, respectively, based on calculations using ab initio density functional theory (DFT) (see Suppl. Sec. S2). Moiré bands derive from either states near the Γ point or the $\pm K$ points. Doped carriers that occupy the moiré valence band arising from $\pm K$ form a two-dimensional triangular lattice. In contrast, the holes in the moiré band derived from Γ form a honeycomb lattice with inequivalent A and B sites (see Fig. 1e). In addition, the moiré bands inherit the contrasting properties of the different Brillouin zone locations. Holes in the K -derived bands are highly localised in one of the WSe_2 layers as shown by the layer distribution of the hole wavefunction (see Suppl. Fig. S9) while Γ holes are delocalised across both WSe_2 layers. The Γ_A band is the lowest energy available valence moiré band. In each sample, optically excited electron-hole pairs reside in $\pm K$ -derived bands, while carriers that dress the excitons are doped into the lowest energy available valence band, which can be either $\pm K$ -derived or Γ -derived. According to the selection rules, for the HTL, σ^+ (σ^-) light probes the $+K$ ($-K$) derived states in L1 and the $-K$ ($+K$) derived states in L2 of the natural bilayer WSe_2 , due to the $2H$ stacking and spin-layer locking [37, 38].

PROBING Γ VALLEY CORRELATED ELECTRONIC STATES VIA EXCITON-POLARON SPECTROSCOPY

Figure 2a,b shows the σ^+ - and σ^- -resolved ν_h dependence of the $d(\Delta R/R_0)/dE$ signal, respectively, in the HTL under application of 5 T magnetic (B) field. The solid lines indicate integer values of ν_h (i.e. the total number of holes per moiré unit cell). To further highlight the formation of correlated electronic states, we plot the derivative of the reflection contrast with respect to V_g , $d(\Delta R/R_0)/dV_g$, as shown in Fig. 2c,d. We note the largest changes in $d(\Delta R/R_0)/dV_g$ (at $V_g = -1.1$ V,

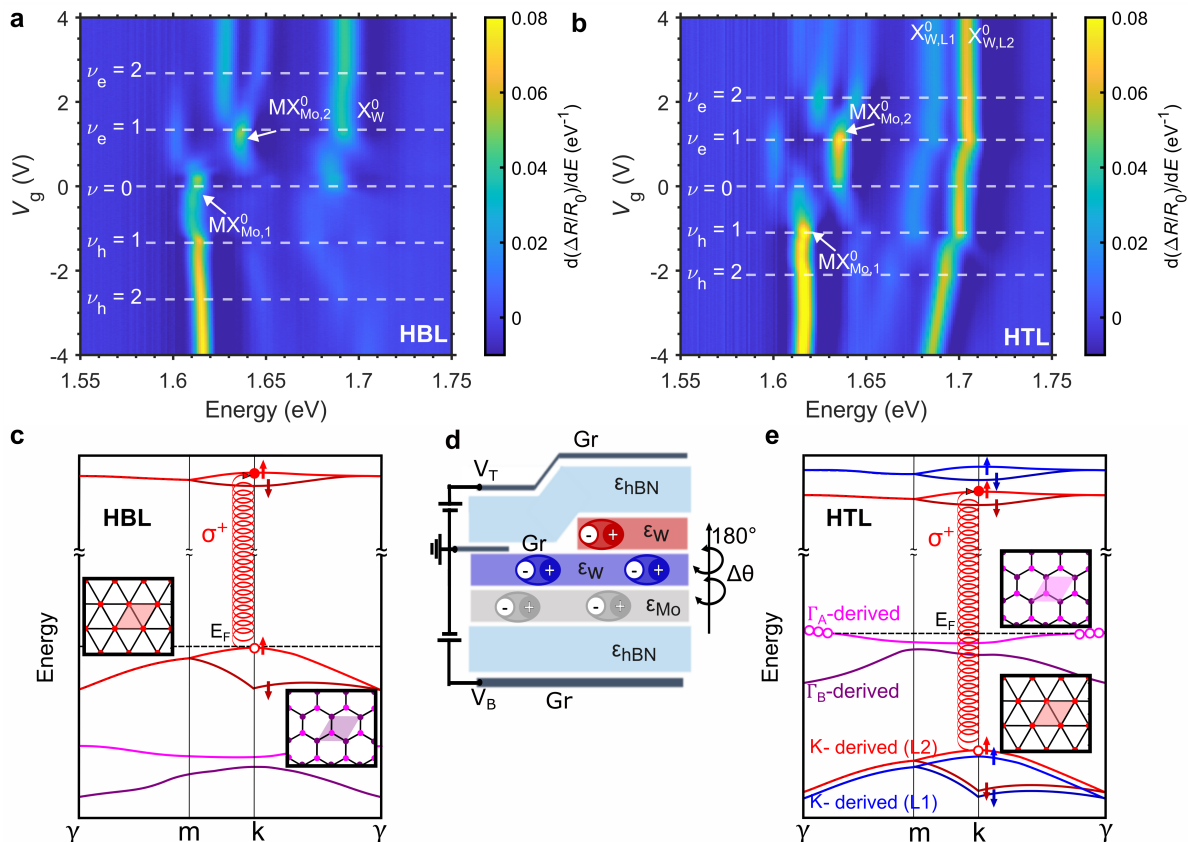


FIG. 1. Layer and valley properties of the excitons and holes in a moiré heterotrilayer device. **a,b**, Density plots of the V_g dependence of $d(\Delta R/R_0)/dE$ in the (a) 1L WSe₂/1L MoSe₂ (HBL) and (b) 2L WSe₂/1L MoSe₂ (HTL) heterostructure regions. The MoSe₂ moiré excitons, $MX_{Mo,1}^0$ and $MX_{Mo,2}^0$, and WSe₂ neutral excitons, $X_{W,L1}^0$ and $X_{W,L2}^0$, are indicated. In the HTL, the intralayer excitons localised in the interface (L1) and upper (L2) layers of the bilayer WSe₂ are non-degenerate due to different dielectric environments (ϵ), as indicated in panel (d). The white dashed lines indicate integer values of electrons and holes per moiré unit cell, ν_e and ν_h , respectively. **d** Schematic of the full device with HBL and HTL regions. The TMD layers are fully encapsulated in hexagonal boron nitride (hBN). Graphene (Gr) layers form contacts to the top and bottom hBN and the heterostructure. **c,e** Band structure schematics for the moiré Brillouin zone based on DFT calculations in the (c) HBL and (e) HTL regions. In the HBL, optically injected excitons reside in $\pm K$ -derived states and are dressed solely by holes in $\pm K$ moiré orbitals. In the HTL, the excitons are dressed by holes at both Γ and $\pm K$ moiré bands. As indicated in the insets, the Γ moiré orbitals form a honeycomb lattice with inequivalent A and B sites. The moiré orbitals from the $\pm K$ valleys form a triangular lattice.

-2.1 V, and -3.1 V) identify the formation of different insulating correlated hole states. Consistent with previous works [11, 16, 20], we use these V_g values to define the number of holes per moiré unit cell, $\nu_h = 1, 2, 3$. We also observe changes in $d(\Delta R/R_0)/dV_g$ at further intermediate hole fillings (black dashed lines in Fig. 2c,d), which we ascribe to the formation of generalised Wigner crystals. We perform temperature-dependent sweeps of V_g while monitoring $\Delta R/R_0$ and find a critical temperature $T_c \sim 98$ K for the correlated state at $\nu_h = 1$ and $T_c \sim 59$ K for the correlated state at $\nu_h = 2$ (see Suppl. Figs. S4 and S5). The V_g required to fill the moiré lattice with either one electron or one hole per site is identical and corresponds to a twist angle of 2.7° (see Methods).

Next, we observe that there is little change in the two WSe₂ excitonic resonance energies as the doping is increased from zero to $\nu_h = 1$. After $\nu_h = 1$, $X_{W,L1}^0$ and $X_{W,L2}^0$ abruptly red-shift, indicating the formation of the hole-dressed attractive polarons $AP_{W,L1}^+$ and $AP_{W,L2}^+$ [32, 39, 40]. Two key pieces of experimental evidence show the valence band maximum in the system derives from the Γ valley, as predicted by the DFT calculations (see Fig. 1e). First, we observe that $AP_{W,L1}^+$ and $AP_{W,L2}^+$ red-shift with increasing ν_h . This is in contrast to natural 2H bilayer WSe₂, where an overall blue-shift of the AP_W^+ occurs due to Pauli blocking effects: resident carriers fill up states at the valence band at the $\pm K$ point where the photo-excited hole also resides [40] (see Suppl.

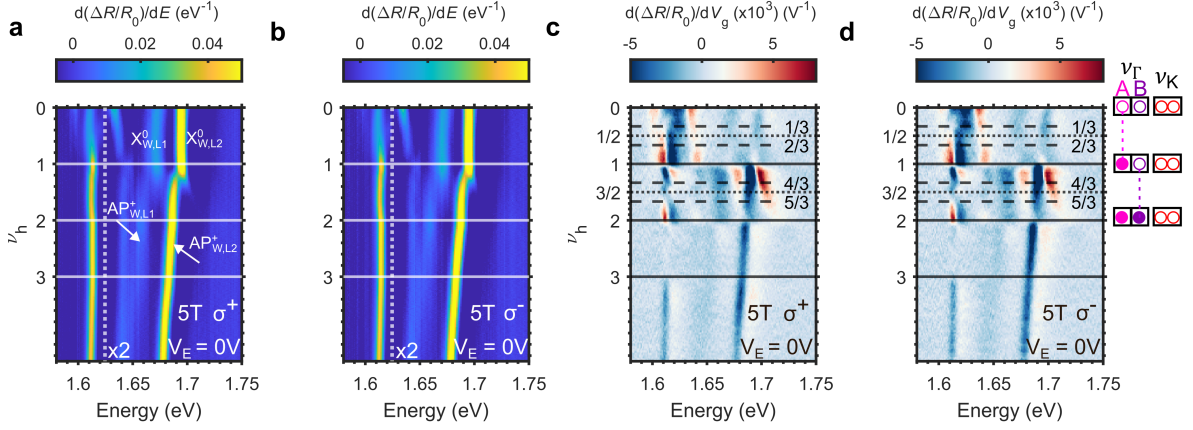


FIG. 2. Γ -valley correlated hole states in the moiré heterotrilayer. **a** σ^+ - and **b** σ^- -helicity-resolved evolution of $d(\Delta R/R_0)/dE$, as a function of ν_h under an applied magnetic field of 5 T. **c,d** Density plot of the first derivative with respect to gate voltage of $\Delta R/R_0$ ($d(\Delta R/R_0)/dV_g$) in panel (a) and (b) respectively. The orbital at the Fermi level is depicted in the schematic to the right. On all plots, the solid lines indicate integer hole fractional fillings of the moiré superlattice, while the dashed and dotted lines in (c,d) show intermediate fractional fillings.

Sec. S1). The contrasting red-shift in the moiré HTL implies that the valence band maximum is *not* derived from $\pm K$ states. Second, unlike the examples of strong spin polarization of holes residing in $\pm K$ valleys [30, 31], in Fig. 2a,b we observe negligible differences in the intensity and energy of $AP_{W,L1}^+$ and $AP_{W,L2}^+$ between the σ^+ - and σ^- -resolved sweeps at an applied magnetic field of 5 T, indicating an absence of a spin-polarisation for the doped holes. This finding is consistent with a photo-excited exciton which resides at $\pm K$ dressed by doped holes in moiré bands derived from the Γ point, in agreement with DFT results. We remark that the formation of $AP_{W,L1}^+$ and $AP_{W,L2}^+$ at the identical V_g value is further evidence of a Γ -derived lowest energy valence band: holes in the Γ band are delocalised across the two WSe_2 layers and dress both $X_{W,L1}^0$ and $X_{W,L2}^0$ equally. In the absence of delocalisation of holes, we would expect carriers to sequentially fill the L1 and L2 derived moiré bands, causing a V_g offset in the formation of $AP_{W,L1}^+$ and $AP_{W,L2}^+$.

We now discuss the nature of the correlated state that arises at $\nu_h = 1$ in the Γ orbital, which is determined to be a charge transfer insulator. The energy gap between the two Γ moiré bands that map onto inequivalent A and B sites of a honeycomb lattice (Γ_A and Γ_B orbitals, respectively) is predicted by DFT to be ~ 18 meV (see Suppl. Sec. S2), comparable to the value of the charge gap we can tentatively estimate from the temperature at which the correlated state at $\nu_h = 1$ disappears, which is ~ 10 meV (see Suppl. Fig. S5). Therefore, the Γ_A lattice is first completely filled, followed by sequential filling of the Γ_B sites. In contrast, for a Mott state, for $1 < \nu_h < 2$ carriers would continue filling the A orbital, leading to doubly occupied sites. The A-B sublattice inequivalency

also presents a likely explanation for the lack of formation of $AP_{W,L1}^+$ and $AP_{W,L2}^+$ up to $\nu_h = 1$. The DFT calculations reveal that the photo-excited hole at K resides on the B sublattice site, while for $0 < \nu_h < 1$ the doped hole in the Γ moiré band lies on the A site (see Suppl. Fig. S9). Hence, there is no spatial or momentum overlap between the two states, minimizing the formation of an attractive exciton-polaron [41]. For $1 < \nu_h < 2$, holes are doped into the Γ_B moiré orbital, which spatially overlaps with the photo-excited hole. Hence, the attractive polarons form in each layer for this range of fractional filling.

ELECTRIC FIELD TUNING OF MOIRÉ ORBITALS

We now investigate the field tunability of the bands. By probing the magneto-optical properties of the WSe_2 exciton-polarons, we disentangle the different spin and valley properties of the holes doped into the Γ and $\pm K$ moiré bands as a function of \vec{E} . Figure 3a,b shows polarisation (σ^+ - and σ^- , respectively)-resolved $d(\Delta R/R_0)/dE$ sweeps as a function of ν_h with $B = 5$ T and $V_E = +3$ V. As we increase ν_h in the σ^- -resolved spectrum (Fig. 3b), a new resonance (labeled $AP_{W,L2}^+$, indicated by the red arrow) appears at $\nu_h = 1$, ~ 14 meV lower energy than $X_{W,L2}^0$. This resonance is notably absent for the σ^+ spectrum (Fig. 3a), where instead the $X_{W,L2}^0$ evolves into the repulsive-polaron branch $RP_{W,L2}^+$ which blueshifts with increasing doping. The difference between the σ^+ and σ^- -resolved sweeps indicates a large degree of spin-polarisation for the carriers that

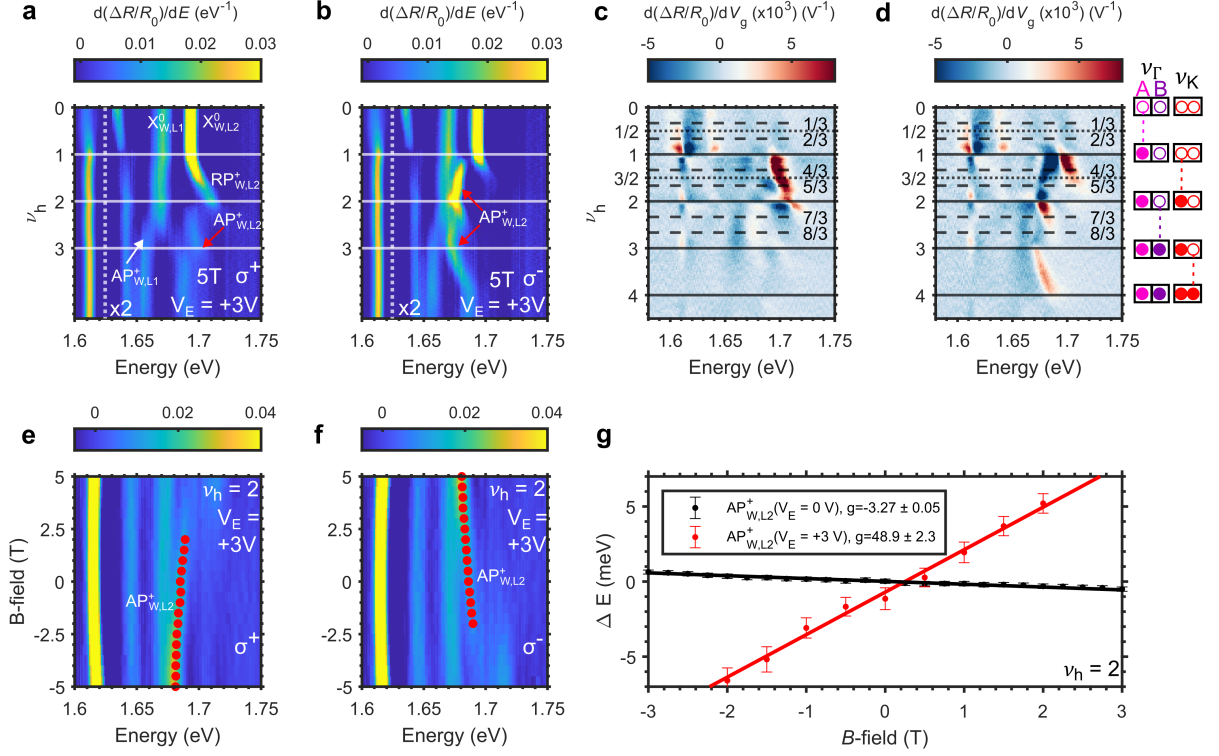


FIG. 3. **Inducing spin and valley polarisation in K orbitals with \vec{E} .** **a,b**, ν_h dependence of the σ^+ (a) and σ^- (b) resolved $d(\Delta R/R_0)/dE$ at $V_E = +3V$ under application of a 5 T magnetic field. **c,d**, Density plot of $d(\Delta R/R_0)/dV_g$ in panel (a) and (b), respectively, which highlight the formation of correlated states, as identified by the dashed and solid lines. The orbital at the Fermi level is depicted in the schematic to the right. **e,f**, σ^+ (e) and σ^- (f) resolved B -field sweep of $d(\Delta R/R_0)/dE$ at $V_E = +3V$ and $\nu_h = 2$. The red dots represent the magnetic-field-dependent estimated energies of the $AP_{W,L2}^+$. **g** B -field-dependent Zeeman splitting, ΔE , of $AP_{W,L2}^+$ at representative hole $\nu_h = 2$ values for $V_E = 0V$ (black dots) and $V_E = +3V$ (red dots). For $V_E = +3V$, ΔE is extracted from the estimated positions shown in panels (e,f). The g -factor of $AP_{W,L2}^+$ is extracted from linear fits to ΔE (solid lines).

form the exciton-polarons in L2. We therefore unambiguously identify $AP_{W,L2}^+$ as the inter-valley attractive polaron which is formed from the direct $\pm K$ exciton in L2 dressed with holes in the opposite K valley in L2 [42, 43]. On application of the positive magnetic field, the valence band edge in L2 at $-K$ is shifted to higher energy relative to $+K$ [42–44]. Exchange interactions favour single valley occupancy of carriers: all the holes are doped into the $-K$ rather than $+K$ valley, leading to the clear spin-polarisation [30]. When we probe the exciton in $+K$ using σ^- light, there is a large population of holes available to form the attractive polaron. In contrast, there is no population of holes at $+K$ available to form the attractive polaron when we probe the $-K$ exciton using σ^+ . This observation strongly indicates that at $V_E = +3V$, the L2 K-derived band is tuned upwards in energy relative to the layer hybridised Γ_B band. Previously, for $V_E = 0V$ and holes loaded only at Γ , there is a complete lack of hole spin-polarisation, regardless of the fractional filling (see

Fig. 2a,b).

Next, we investigate the interaction effects on the magneto-optics for the correlated states in the Γ and K orbitals. Figure 3e and 3f show the σ^- - and σ^+ -helicity-resolved evolution of the $d(\Delta R/R_0)/dE$ spectrum for applied B -fields between $-5T$ and $5T$ at $\nu_h = 2$ and $V_E = +3V$. The B -field-dependent estimated energy of $AP_{W,L2}^+$ extracted from fits are overlaid (red dots). Figure 3g shows the Zeeman splitting, ΔE , of $AP_{W,L2}^+$ versus B -field at $\nu_h = 2$, for both $V_E = 0V$ (black) and $V_E = +3V$ (red), where $\Delta E = E^{\sigma^+} - E^{\sigma^-}$, with E^{σ^\pm} the energy of the transition with σ^\pm polarisation. The evolution of ΔE with B -field can be associated with an effective exciton g -factor, g , using $\Delta E(B) = g\mu_0 B$, where μ_0 is the Bohr magneton. For $V_E = 0V$, when $AP_{W,L2}^+$ is formed by an exciton dressed by holes at Γ , the g -factor is close to -4 , which is expected according to spin and valley considerations in the absence of interaction effects [45]. In contrast, for $V_E = +3V$, $AP_{W,L2}^+$ exhibits a large

positive g -factor, ~ 49 , partly due to the aforementioned interaction effects that arise from hole doping into the $\pm K$ band and the resulting favoured single valley occupancy (see Suppl. Fig. S3 and Suppl. Tab. S2) [30]. The measured g -factor is then further enhanced by spin-coupling between the moiré localised holes [16, 20].

The tuning of the valence bands in the system is further demonstrated by the suppression of the formation of the attractive polaron for the L1 WSe₂ exciton, AP_{L1}^+ , up to $\nu_h > 2$: holes are doped into the highly localised K-L2 band and therefore have little effect on the L1 WSe₂ exciton. Finally, we note that the binding energy, E_B , for the hole-dressed attractive polaron formed by the L2-localised exciton for $V_E = +3$ V ($E_B \sim 14$ meV) is much larger than the binding energy for $V_E = 0$ V ($E_B \sim 6$ meV). This result is consistent with a larger wavefunction overlap between the exciton at $\pm K$ dressed by holes at $\mp K$ compared to holes at Γ .

CORRELATED STATES: Γ VERSUS K ORBITALS

We now investigate the correlated states formed within the Γ and K orbitals. We expect the same dependence of V_g versus ν_h for each orbital. Figure 3c,d, shows the ν_h dependence of $d(\Delta R/R_0)/dV_g$ for the same data in panels (a) and (b), respectively. As expected, we observe the largest changes in the $d(\Delta R/R_0)/dV_g$ signal at integer ν_h and further smaller changes at intermediate ν_h , as previously observed for $V_E = 0$ V (see Fig. 2c,d). However, we observe that new correlated states emerge for $V_E = +3$ V compared to $V_E = +0$ V. A new state at $\nu_h = 4$ clearly appears, as well as further states at $\nu_h = 7/3$ and $8/3$.

To understand the origin of the additional correlated insulating states, we again use the polarisation-resolved doping-dependent reflection contrast measurements (see Fig. 2a,b and Fig. 3a,b), and assign the correlated states to filling of either the Γ or K orbitals, as indicated by the schematics at the far right of the figures. For $\nu_h < 1$, we observe that attractive polarons do not form for any V_E because holes are always first doped into the Γ_A orbital. We then observe that $AP_{W,L2}^+$ and $RP_{W,L2}^+$ form at $\nu_h > 1$ with a large spin-polarisation demonstrating doping into the K orbital. Hence, for $V_E = +3$ V at $\nu_h = 2$, a correlated state arises in which the lower Hubbard bands are filled for both the Γ_A and K orbitals. In contrast, for $V_E = 0$ V and $1 < \nu_h < 2$, the Γ_B orbital is filled, as demonstrated by the lack of spin-polarisation of the carriers that form $AP_{W,L1}^+$ and $AP_{W,L2}^+$ (see Fig. 2a,b).

Continuing with the $V_E = +3$ V scenario, after $\nu_h = 2$ the non-spin-polarised $AP_{W,L1}^+$ forms because holes are now doped into the Γ_B orbital. Hence, at $\nu_h = 3$, a correlated state arises in which each orbital (Γ_A , Γ_B , and K) is filled with one hole. Finally for $\nu_h > 3$, $AP_{W,L2}^+$ continually blueshifts with increasing doping, indicating Pauli blocking effects arising from doping into the K or-

bit, whereas $AP_{W,L1}^+$ remains unaffected. At $\nu_h = 4$, we therefore have a correlated state with $\nu_\Gamma = 2$ and $\nu_K = 2$. These assignments are consistent with the emergence of new states at $\nu_h = 7/3$ and $8/3$ for $V_E + 3$ V. In comparison, for $V_E = 0$ V, the Wigner crystals driven by long-range interactions are not observed at these fractional fillings of the moiré lattice in the next Γ moiré orbital, either due to more disorder or weaker correlations (increased bandwidth). The emergence of new correlated states at $\nu_h = 7/3, 8/3$ and 4 is consistent with metal-to-insulator transitions occurring at these fractional fillings, driven by V_E -dependent tuning of the relative Γ -K band energies.

THE INTERPLAY OF CORRELATED STATES BETWEEN DEGENERATE ORBITALS

To better understand the different V_E -dependent shifts in the K and Γ_B orbitals, we perform DFT calculations for the HTL in the presence of a vertical electric field. Figure 4a shows a simplified band structure schematic in the moiré Brillouin zone for a positive vertical electric field (see Suppl. Fig. S10) for calculated full band structure). In agreement with the experimental results, we observe that the $\pm K$ -derived bands which are localized on L2 are pushed up in energy (i.e. reduced hole energy) relative to the Γ_B bands (see Fig. 1e for a comparison). Fig. 4b shows the band-edge energy of the Γ_A , Γ_B , K-L1, and K-L2 bands as function of the applied electric field strength. Due to the high localisation of its wavefunction on L2 WSe₂ (see Suppl. Fig. S10), the K-L2 orbital exhibits the largest V_E dependent shift in energy. In contrast, the Γ_A and Γ_B bands exhibit smaller V_E dependent energy shifts due to the delocalisation across both WSe₂ layers[34].

To probe the interplay between correlated states in Γ and K orbitals in more detail, we measure the V_E dependence of the $d(\Delta R/R_0)/dE$ signal for a fixed hole filling of $\nu_h = 2$ (see Fig. 4c). For $V_E = 0$ V, we observe the two WSe₂ attractive polaron resonances: intralayer excitons localised in L1 and L2 of the bilayer dressed by delocalised holes residing in the highest Γ moiré mini-band ($AP_{W,L1}^+$ and $AP_{W,L2}^+$, respectively). However, as V_E is increased, these features are abruptly replaced by 3 new resonances at $V_E \sim 2.3$ V, indicated by the vertical white dashed line. The full width half maximum of the change in the $d(\Delta R/R_0)/dE$ signal is calculated to be $\Delta V_E = 0.53$ V (see Suppl. Fig. S2). To identify the origin of the abrupt change in the excitonic resonances, we measure the σ^+ - and σ^- - resolved ν_h dependence of the $d(\Delta R/R_0)/dE$ signal, respectively, with $V_E = +2$ V (near the abrupt transition in Fig. 4c) and $B = 5$ T (see Fig. 4d,e). Figure 4f,g, shows the ν_h dependence of $d(\Delta R/R_0)/dV_g$ for the data in panels (d) and (e), respectively. Here, the large change at $\nu_h = 2$

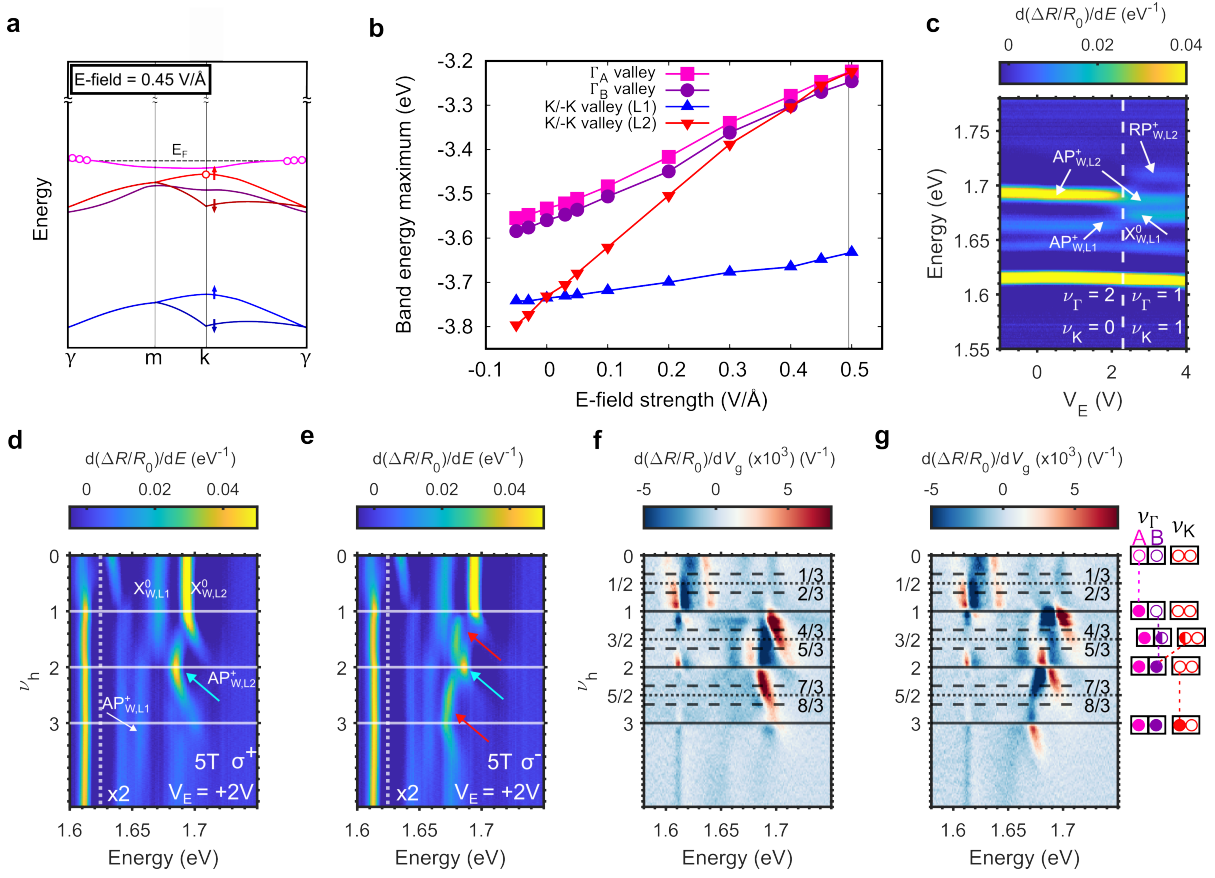


FIG. 4. Interplay of K and Γ correlated states. **a** Band structure schematic for the moiré Brillouin zone based on DFT calculations of the heterotrilaier under an applied positive vertical electric field. The K-derived band is shifted to higher energy relative to the Γ -derived bands compared to $V_E = 0$. **b** Electric field dependence of the valence band maximum for the Γ and K-derived moiré bands, calculated from DFT. **c** Density plot of the V_E dependence of the derivative of the $d(\Delta R/R_0)/dE$ when the hole filling is fixed at $\nu_h = 2$. The white dashed line indicates an abrupt transfer of holes in the system from the Γ -derived moiré orbital to the K-derived orbital. **d,e** ν_h dependence of the σ^+ (**d**) and σ^- (**e**) resolved $d(\Delta R/R_0)/dE$ at $V_E = +2$ V under application of a 5 T magnetic field. **f,g** Density plot of $d(\Delta R/R_0)/dV_g$ for the same data in panels (**d**) and (**e**), respectively. On all plots, the solid lines indicate integer hole fractional fillings of the moiré superlattice, while the dashed and dotted lines in (**f,g**) show intermediate fractional fillings. The schematics on the far right indicate the carriers per moiré unit cell in each of the Γ -derived or K-derived orbitals, where a filled circle indicates integer filling.

in $d(\Delta R/R_0)/dV_g$ indicates strongly correlated state formation. Identical to the case for $V_E = +3$ V, in the σ^- spectrum (Fig. 4d) we observe the emergence of a new highly spin-polarised resonance $AP_{W,L2}^+$ (red arrow), indicating holes are initially doped into the L2 K moiré band for $\nu_h > 1$. However, for σ^- , around $\nu_h = 2$ the oscillator strength is transferred to a higher energy feature with a smaller binding energy, which also appears for the σ^+ -resolved data (indicated by the blue arrows). This feature lacks a strong degree of spin-polarisation, suggesting that holes are transferred from the K to the Γ_B orbital at $\nu_h = 2$. The hole transfer is further demonstrated by the formation of the attractive polaron for the L1 WSe₂ exciton around $\nu_h = 2$, at the same hole filling where the oscillator strength transfer occurs. For $\nu_h > 2$, holes start to be doped into the K orbital again,

and the spin-polarised features re-emerge. Therefore, we assign the abrupt change in the the absorption spectrum at $V_E = +2.3$ V in Fig. 4c to a transfer of holes from the Γ_B to the K moiré orbital.

Rather than being continuous, the observed change occurs over a small range of V_E ($\Delta V_E \sim 0.5$ V). If holes were continuously transferred between the orbitals there would be a gradual change in oscillator strength [18]. Instead, the abrupt change indicates that the system favours correlated state formation, and the different V_E -dependent scenarios for $\nu_h = 2$ provide an archetypal illustration. For small V_E , a correlated state with $\nu_h = 1$ in each Γ_A and Γ_B orbital arises. For large V_E , a correlated state with $\nu_h = 1$ in the Γ_A orbital and $\nu_h = 1$ in the K orbital is formed. However, when the Γ_B and K orbitals are nearly degenerate at the Fermi level, the

holes preferentially transfer from the K orbital to the Γ_B orbital, likely due to a larger Coulomb gap for the filled Γ_B orbital which minimises the energy of the correlated state. A summary of the orbital filling near degeneracy is depicted in the schematic to the right of Fig. 4g.

DISCUSSION

In the experiment, we observe an interplay between correlated states in three orbitals which can be tuned with V_E . Here we develop a theoretical model to provide a more detailed picture of the charge ordering and interactions of these correlated states. Charges can be distributed (and redistributed) between the Γ_A , Γ_B , and K orbitals as hole filling is increased. It is likely that complex correlated states with specific charge ordering in real space arise to minimise electrostatic repulsion for a given ν_h , similar to that observed in bilayer Hubbard model physics [21].

We analyze a three-orbital t - U - \mathcal{V} Hamiltonian in the $t/U \rightarrow 0$ limit. In this limit, each moiré site can be occupied by at most one hole and no hopping between moiré sites is allowed. To find the configuration of holes n_i (where i labels the various moiré sites corresponding to L2 K, Γ_A , and Γ_B orbitals) which minimizes the total energy, we use a Monte Carlo simulated annealing approach. The total energy is given by

$$H = \varepsilon_A \sum_{i \in \Gamma_A} n_i + \varepsilon_B \sum_{i \in \Gamma_B} n_i + \varepsilon_K(V_E) \sum_{i \in K} n_i + \frac{1}{2} \sum_{i,j \in \{\Gamma_A, \Gamma_B, K\}} \mathcal{V}(|\mathbf{r}_i - \mathbf{r}_j|) n_i n_j, \quad (1)$$

where ε_A , ε_B and $\varepsilon_K(V_E)$ denote the onsite energies of the Γ_A , Γ_B , and L2 K orbitals, respectively. Note that the onsite energy of the L2 K orbital (relative to that of the Γ orbitals) depends on the applied electrostatic potential V_E . From our DFT calculations, we estimate $\varepsilon_A - \varepsilon_B \approx 20$ meV, independent of V_E . Also, $\mathcal{V}(|\mathbf{r}_i - \mathbf{r}_j|) = \frac{\exp\{(-|\mathbf{r}_i - \mathbf{r}_j|/L_0)\}}{\epsilon|\mathbf{r}_i - \mathbf{r}_j|}$ denotes the screened Yukawa interaction between holes located at positions \mathbf{r}_i and \mathbf{r}_j , where ϵ is the dielectric constant which we set to 4.5 and L_0 is the characteristic screening length which we set to 2 nm. As the K-derived states are highly localized on the WSe₂ L2 layer, the corresponding hole positions are assumed to lie in the plane of the layer. In contrast, our DFT calculations show that the Γ -derived states are delocalized across both WSe₂ layers and we therefore assume that the corresponding hole positions lie at the midpoint between the layers.

First, we model the trilayer without an electric field, i.e. $V_E = 0$. In this case, ε_K is much larger than both ε_A and ε_B . For $\nu_h = 1$, the holes occupy the Γ_A orbitals, forming a triangular lattice as shown in Fig. 5a.

The electronic structure of this correlated state is characterized by an occupied lower hole Hubbard band which is separated from the upper hole Hubbard band by the onsite Coulomb energy U_{Γ_A} , see Fig. 5a. Further hole doping results in occupancy of the Γ_B sites, and to the formation of charge-ordered Γ_B -states, consistent with the experimental findings of the Γ -derived Wigner crystal at $\nu_h = 4/3$ (shown in Fig. 2c,d). At $\nu_h = 2$, all Γ_A and Γ_B sites are occupied while the L2 K orbital remains empty.

Next, we consider the case of a large electric field, $V_E = +3$ V. In this case, $\varepsilon_B > \varepsilon_K > \varepsilon_A$ and for $\nu_h = 1$ the holes still occupy the Γ_A sites. Further hole doping, however, results in the L2 K orbital becoming occupied and forming charge-ordered states, see Fig. 5b, consistent with the experimental picture of B -field-dependent correlated states at $\nu_h = 4/3$. At $\nu_h = 2$, the lower Hubbard bands of the Γ_A and L2 K orbitals are fully occupied by holes while the upper Hubbard bands are empty.

Finally, we consider the critical electric field, $V_E = +2.3$ V. At this field, the $\varepsilon_B \approx \varepsilon_K > \varepsilon_A$ and we expect strong quantum interaction effects to occur which are not captured by our electrostatic model. For $\nu_h = 1$, the holes still occupy the Γ_A sites. As a result of the degeneracy of the Γ_B and the L2 K-orbitals, we hypothesize that additional holes ($1 < \nu_h < 2$) occupy both orbitals to minimize the overall Coulomb repulsion, see Fig. 5c. When the doping reaches $\nu_h = 2$, we experimentally observe that all holes reside in Γ -derived states. This can be explained by the formation of a correlated state in which the lower Hubbard bands of both Γ_A and Γ_B orbitals are fully occupied. As the bandwidth of the Γ -derived bands is smaller than that of the K-derived bands (according to our DFT calculations), compared to a state in which the L2 K orbital is fully occupied it is energetically favorable for the Γ orbitals to be fully occupied. Thus, the holes spontaneously redistribute from the K to the Γ_B orbital. This observation provides motivation for future theoretical and experimental investigations to fully understand the many-body physics of this strongly correlated multi-orbital system.

CONCLUSIONS

In conclusion, we use exciton-polaron spectroscopy of a moiré HTL device to reveal strongly correlated hole states in Γ and K orbitals that are best described by an extended t - U - \mathcal{V} three-orbital Hubbard model. Notably, we find that the honeycomb Γ -band gives rise to a charge-transfer insulator which also hosts generalized Wigner crystal states at several intermediate fractional fillings. With application of \vec{E} , we change the ordering of the Γ_B - and K-derived bands and observe a sudden transfer of the holes from the correlated states formed in the Γ_B to the K orbital, where new strongly correlated states emerge.

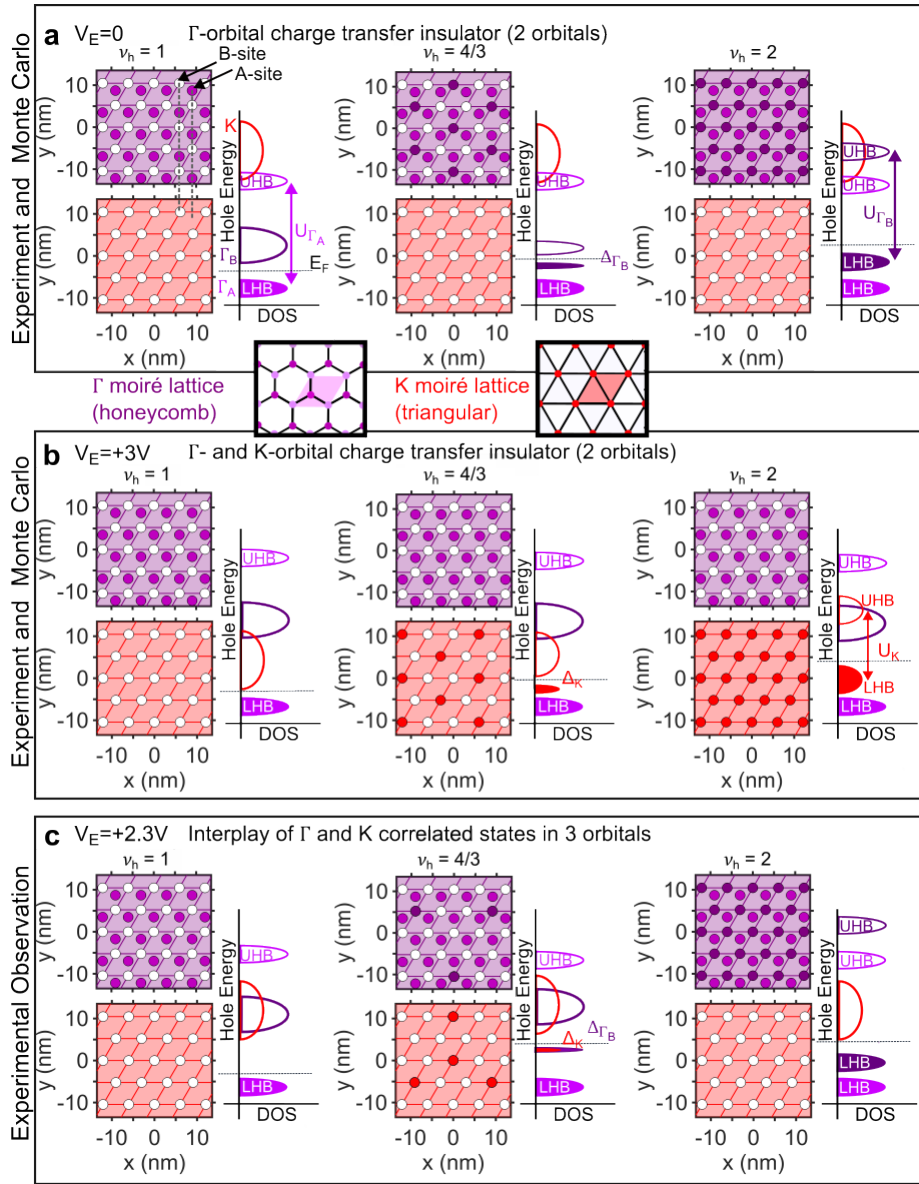


FIG. 5. **Real-space charge distributions of correlated states in the Γ_A , Γ_B , and K orbitals at selected values of ν_h and V_E .** **a** Monte Carlo simulated charge ordered states that arise in the Γ (pink and purple) and K (red) moiré lattices for $V_E = 0$, for which the energy of the K-derived band is below both Γ -derived bands ($\epsilon_K < \epsilon_B$). The Γ_B sites are spatially aligned with the K sites in the $x-y$ plane. Holes are first loaded into the Γ_A sites up to $\nu_h = 1$ and into the Γ_B sites for $\nu_h > 1$. Schematics to the right illustrate the hole energy versus density of states (DOS) for each charge ordered state depicted. Lower and upper Hubbard bands (LHB and UHB) form for $\nu_h = 1$, while a charge gap Δ opens for correlated states that form for non-integer filling. **b** Monte Carlo simulated charge ordered states and corresponding DOS schematics that arise for $V_E = +3$ V, for which the energy of the K orbital lies between the Γ orbitals ($\epsilon_A > \epsilon_K > \epsilon_B$). Holes are first loaded into the Γ_A sites up to $\nu_h = 1$, and into K for $\nu_h > 1$. **c** Experimentally observed charge ordered states and corresponding DOS schematics for $V_E = +2.3$ V for which the K orbital is energetically degenerate with the Γ_B orbital. Holes are first loaded into the Γ_A sites up to $\nu_h = 1$, and into both K and Γ_B for $\nu_h > 1$. At $\nu_h = 2$ holes are abruptly transferred from K to Γ_B to form the correlated state with $\nu_{\Gamma_A} = 1$ and $\nu_{\Gamma_B} = 1$.

Further, in the critical condition when Γ_B and K are degenerate at the Fermi level, we observe stable correlated states simultaneously in each orbital at non-integer fractional fillings (between $1 < \nu_h < 2$). However, upon approaching $\nu_h = 2$, the holes abruptly redistribute from

the K to the Γ_B orbital, likely due to a larger Coulomb gap for the filled Γ_B orbital which minimises the energy of the correlated state.

Our work establishes the HTL as a platform for investigation of both honeycomb and triangular Hubbard

systems, as well as their interplay [7]. Exploring the magnetic phase diagrams of the charge transfer insulating states [15, 46] and honeycomb lattice Wigner crystals [23, 24] are exciting future avenues to pursue. Further, the high tunability and large number of degrees of freedom available in this system could enable the exploration of Kondo interactions when $\nu_h = 1$ in the lowest Hubbard band while a higher energy, more dispersive orbital is partially filled [47, 48].

METHODS

Exciton-Polaron Spectroscopy of Correlated States With Layer and Valley Specificity

To precisely probe the nature of the correlated states, we develop an optical spectroscopy technique that yields unambiguous layer and valley specific experimental signatures. We probe momentum-direct electrons and holes at $\pm K$ valleys that form tightly-bound intralayer excitons which are extremely sensitive to their environment. The exciton binding energy depends on its dielectric environment [49], leading to layer specific exciton energies [50], while excitons dressed by a Fermi sea form attractive (AP) and repulsive (RP) exciton-polarons [31, 51–53] which exhibit distinct behaviours depending on the valley hosting the Fermi sea. For doping at $\pm K$, dominant phase space filling effects cause an overall blue-shift in the AP [30, 54] while doping in the Γ valley leads to a continuous red-shift due to bandgap renormalisation [55, 56]. Contrasting properties in an applied magnetic field also manifest for excitons dressed by carriers in the two valleys: unlike Γ -valley holes, K -valley holes are highly spin-polarised and exhibit strong magnetic interactions with excitons at $\pm K$ [30]. Finally, the formation of strongly correlated states leads to abrupt changes in the oscillator strength, energy, and linewidth of the exciton polarons, regardless of which valley the Fermi-sea occupies [16, 18, 20]. Altogether, exciton-polarons provide probes of strongly correlated electronic states with layer and valley specificity.

Device Details

The heterostructure is fully encapsulated in hexagonal boron nitride (hBN). There are few layer graphene contacts to both the top and bottom hBN, as well as the heterostructure which allows the carrier concentration and vertical electric field to be tuned independently (see Fig. 1b). To change the carrier concentration in the heterostructure, without changing the vertical electric field, we sweep both V_T and V_B with the same values, i.e. $V_T = V_B = \Delta V_g$. To change the vertical electric field without changing the carrier concentration,

$V_T = -V_B = V_E$. The applied vertical electric field can then be calculated using $E = \frac{(V_T - V_B)}{(d_1 + d_2)} \frac{\epsilon_{hBN}}{\epsilon_{TMD}}$. For intermediate regimes, when we want to change both the applied vertical electric field *and* the carrier concentration, we apply asymmetric gating, i.e. $V_T \neq V_B$ [57].

The carrier concentration n in the heterostructure can be calculated using the parallel plate capacitance model, $n = \frac{\epsilon \epsilon_0 \Delta V_g}{d_1} + \frac{\epsilon \epsilon_0 \Delta V_g}{d_2}$ where ϵ is the permittivity of hBN, ΔV_g is the voltage offset between both the top and bottom gates and the heterostructure gate, and d_1 (d_2) is the thickness of the top (bottom) hBN layer measured to be 17.4 ± 0.2 nm (18.2 ± 0.3 nm) using nulling ellipsometry. For a small angular difference between two stacked layers the moiré periodicity can be estimated using $\lambda_M = \frac{a_{Se}}{\sqrt{\delta^2 + \theta^2}}$ where a_{Se} is the lattice constant of WSe₂, δ is the fractional lattice mismatch between the two layers and θ is the twist angle in radians. For a triangular moiré pattern (or honeycomb with inequivalent A and B sites, where only one site is doped), the number of carriers required for one hole per site is given by $n_0 = \frac{2}{\sqrt{3}\lambda_M^2}$. Using the lattice constants of 0.3280 nm and 0.3288 nm for WSe₂ and MoSe₂ respectively [58] and a permittivity of 3.8 for the hBN [59], and $\Delta V_g = 1.00$ V for $\nu_h = 1$ as determined in the main text, we calculate the twist angle in the main measurement location to be 2.7° . We determine the interface in the HTL is R-stacked, as a result of the fabrication process. Single flakes of MoSe₂ and WSe₂ with monolayer and natural 2H bilayer regions are first exfoliated with the terraced layers (flat surface) facing up (on the substrate). The WSe₂ flake (terraced side up) is then transferred onto the MoSe₂ on its substrate, keeping the interface between the two layers free from contaminants. The HBL region is H-stacked, as demonstrated by magneto-optical studies on the same sample [60, 61] while in the HTL region the WSe₂ interface layer L1 is R-stacked relative to the MoSe₂ monolayer. The upper WSe₂ layer L2 is therefore H-stacked relative to the monolayer MoSe₂. We note that second harmonic generation measurements cannot be used to determine R- versus H-stacking of the hetero-interface of the HTL.

Optical Spectroscopy Measurements

We focus a broadband white light source from a power-stabilised halogen lamp onto the sample, and measure the reflected signal in a liquid nitrogen cooled CCD spectrometer. The sample is mounted in a closed-cycle cryostat and the sample temperature for all experiments in the main text is 4 K. We define reflection contrast as $\Delta R/R_0$, where $\Delta R = (R_S - R_0)/R_0$. Here R_S is the reflected signal from the heterostructure, and R_0 is the reflected signal from a nearby heterostructure region without the TMD layers.

DFT calculations

The moiré unit cell for the free-standing $2H$ $\text{WSe}_2/\text{MoSe}_2$ heterotrilinear with a twist angle of 3.1° contains 2979 atoms. To calculate the band structure, we first relax the atomic positions using classical force fields as implemented in the LAMMPS code [62] (see Suppl. Sec. S2 for details on the heterotrilinear geometry and atomic relaxations). DFT calculations were carried out on the relaxed structure using the linear-scaling DFT code SIESTA [63]. We employ the LDA exchange-correlation functional [64], with a double-zeta plus polarization (DZP) pseudoatomic orbitals basis set, a mesh cutoff of 300 Ry and a vacuum region between periodic images of 15 Å. Spin-orbit coupling was included via the “on-site” approximation [65]. Electron-ion interactions are described by fully relativistic Troulliers-Martins pseudopotentials [66]. For the calculations with a non-zero vertical electric field, the same atomic positions as in the zero-field case are used and we employ a slab dipole correction, in which the electric field used to compensate the dipole of the system is computed self-consistently in every iteration [67]. DFT band structures with and without the electric field as well as selected wavefunctions of Γ -valley and $\pm K$ -valley bands are reported in Suppl. Sec. S2.

* B.D.Gerardot@hw.ac.uk

- [1] VJ Emery, “Theory of high- T_c superconductivity in oxides,” *Physical Review Letters* **58**, 2794 (1987).
- [2] FC Zhang and TM Rice, “Effective Hamiltonian for the superconducting Cu oxides,” *Physical Review B* **37**, 3759 (1988).
- [3] Elbio Dagotto, “Correlated electrons in high-temperature superconductors,” *Reviews of Modern Physics* **66**, 763 (1994).
- [4] Pengcheng Dai, Jiangping Hu, and Elbio Dagotto, “Magnetism and its microscopic origin in iron-based high-temperature superconductors,” *Nature Physics* **8**, 709–718 (2012).
- [5] G Rohringer, H Hafermann, A Toschi, AA Katanin, AE Antipov, MI Katsnelson, AI Lichtenstein, AN Rubtsov, and K Held, “Diagrammatic routes to nonlocal correlations beyond dynamical mean field theory,” *Reviews of Modern Physics* **90**, 025003 (2018).
- [6] Christian Gross and Immanuel Bloch, “Quantum simulations with ultracold atoms in optical lattices,” *Science* **357**, 995–1001 (2017).
- [7] Dante M Kennes, Martin Claassen, Lede Xian, Antoine Georges, Andrew J Millis, James Hone, Cory R Dean, DN Basov, Abhay N Pasupathy, and Angel Rubio, “Moiré heterostructures as a condensed-matter quantum simulator,” *Nature Physics* **17**, 155–163 (2021).
- [8] Leon Balents, Cory R Dean, Dmitri K Efetov, and Andrea F Young, “Superconductivity and strong correlations in moiré flat bands,” *Nature Physics* **16**, 725–733 (2020).
- [9] Kin Fai Mak and Jie Shan, “Semiconductor moiré materials,” *Nature Nanotechnology* **17**, 686–695 (2022).
- [10] Augusto Ghiotto, En-Min Shih, Giancarlo SSG Pereira, Daniel A Rhodes, Bumho Kim, Jiawei Zang, Andrew J Millis, Kenji Watanabe, Takashi Taniguchi, James C Hone, *et al.*, “Quantum criticality in twisted transition metal dichalcogenides,” *Nature* **597**, 345–349 (2021).
- [11] Tingxin Li, Shengwei Jiang, Lizhong Li, Yang Zhang, Kaifei Kang, Jiacheng Zhu, Kenji Watanabe, Takashi Taniguchi, Debanjan Chowdhury, Liang Fu, *et al.*, “Continuous mott transition in semiconductor moiré superlattices,” *Nature* **597**, 350–354 (2021).
- [12] Petr Stepanov, Ipsita Das, Xiaobo Lu, Ali Fahimniya, Kenji Watanabe, Takashi Taniguchi, Frank HL Koppens, Johannes Lischner, Leonid Levitov, and Dmitri K Efetov, “Untying the insulating and superconducting orders in magic-angle graphene,” *Nature* **583**, 375–378 (2020).
- [13] Tingxin Li, Jiacheng Zhu, Yanhao Tang, Kenji Watanabe, Takashi Taniguchi, Veit Elser, Jie Shan, and Kin Fai Mak, “Charge-order-enhanced capacitance in semiconductor moiré superlattices,” *Nature Nanotechnology* **16**, 1068–1072 (2021).
- [14] Fengcheng Wu, Timothy Lovorn, Emanuel Tutuc, and Allan H MacDonald, “Hubbard model physics in transition metal dichalcogenide moiré bands,” *Physical Review Letters* **121**, 026402 (2018).
- [15] Yang Zhang, Noah FQ Yuan, and Liang Fu, “Moiré quantum chemistry: charge transfer in transition metal dichalcogenide superlattices,” *Physical Review B* **102**, 201115 (2020).
- [16] Yanhao Tang, Lizhong Li, Tingxin Li, Yang Xu, Song Liu, Katayun Barmak, Kenji Watanabe, Takashi Taniguchi, Allan H MacDonald, Jie Shan, *et al.*, “Simulation of Hubbard model physics in WSe_2/WS_2 moiré superlattices,” *Nature* **579**, 353–358 (2020).
- [17] Emma C Regan, Danqing Wang, Chenhao Jin, M Iqbal Bakti Utama, Beini Gao, Xin Wei, Sihan Zhao, Wenyu Zhao, Zuo Cheng Zhang, Kentaro Yumigeta, *et al.*, “Mott and generalized Wigner crystal states in WSe_2/WS_2 moiré superlattices,” *Nature* **579**, 359–363 (2020).
- [18] Yuya Shimazaki, Ido Schwartz, Kenji Watanabe, Takashi Taniguchi, Martin Kroner, and Ataç Imamoğlu, “Strongly correlated electrons and hybrid excitons in a moiré heterostructure,” *Nature* **580**, 472–477 (2020).
- [19] Lei Wang, En-Min Shih, Augusto Ghiotto, Lede Xian, Daniel A Rhodes, Cheng Tan, Martin Claassen, Dante M Kennes, Yusong Bai, Bumho Kim, *et al.*, “Correlated electronic phases in twisted bilayer transition metal dichalcogenides,” *Nature materials* **19**, 861–866 (2020).
- [20] Aidan J Campbell, Mauro Brotons-Gisbert, Hyeonjun Baek, Valerio Vitale, Takashi Taniguchi, Kenji Watanabe, Johannes Lischner, and Brian D Gerardot, “Exciton-polarons in the presence of strongly correlated electronic states in a $\text{MoSe}_2/\text{WSe}_2$ moiré superlattice,” *npj 2D Materials and Applications* **6**, 1–8 (2022).
- [21] Yang Xu, Kaifei Kang, Kenji Watanabe, Takashi Taniguchi, Kin Fai Mak, and Jie Shan, “A tunable bilayer Hubbard model in twisted WSe_2 ,” *Nature Nanotechnology* **17**, 934–939 (2022).
- [22] Mattia Angeli and Allan H MacDonald, “ Γ valley transition metal dichalcogenide moiré bands,” *Proceedings of the National Academy of Sciences* **118**, e2021826118

- (2021).
- [23] Ledex Xian, Martin Claassen, Dominik Kiese, Michael M Scherer, Simon Trebst, Dante M Kennes, and Angel Rubio, “Realization of nearly dispersionless bands with strong orbital anisotropy from destructive interference in twisted bilayer MoS_2 ,” *Nature Communications* **12** (2021).
- [24] Nitin Kaushal, Nicolás Morales-Durán, Allan H MacDonald, and Elbio Dagotto, “Magnetic ground states of honeycomb lattice Wigner crystals,” *Communications Physics* **5**, 289 (2022).
- [25] Liheng An, Xiangbin Cai, Ding Pei, Meizhen Huang, Zefei Wu, Zishu Zhou, Jiangxiazi Lin, Zhehan Ying, Ziqing Ye, Xuemeng Feng, *et al.*, “Interaction effects and superconductivity signatures in twisted double-bilayer WSe_2 ,” *Nanoscale Horizons* **5**, 1309–1316 (2020).
- [26] Ding Pei, Binbin Wang, Zishu Zhou, Zhihai He, Liheng An, Shanmei He, Cheng Chen, Yiwei Li, Liyang Wei, Aiji Liang, *et al.*, “Observation of Γ -valley moiré bands and emergent hexagonal lattice in twisted transition metal dichalcogenides,” *Physical Review X*, 021065 (2022).
- [27] Gianmarco Gatti, Julia Issing, Louk Rademaker, Florian Margot, Tobias A de Jong, Sense Jan van der Molen, Jérémie Teyssier, Timur K Kim, Matthew D Watson, Cephise Cacho, *et al.*, “Observation of flat Γ moiré bands in twisted bilayer WSe_2 ,” arXiv preprint arXiv:2211.01192 (2022).
- [28] Benjamin A Foutty, Jiachen Yu, Trithep Devakul, Carlos R Kometter, Yang Zhang, Kenji Watanabe, Takashi Taniguchi, Liang Fu, and Benjamin E Feldman, “Tunable spin and valley excitations of correlated insulators in Γ -valley moiré bands,” arXiv preprint arXiv:2206.10631 (2022).
- [29] Valerio Vitale, Kemal Atalar, Arash A Mostofi, and Johannes Lischner, “Flat band properties of twisted transition metal dichalcogenide homo- and heterobilayers of MoS_2 , MoSe_2 , WS_2 and WSe_2 ,” *2D Materials* **8**, 045010 (2021).
- [30] Patrick Back, Meinrad Sidler, Ovidiu Cotlet, Ajit Srivastava, Naotomo Takemura, Martin Kroner, and Atac Imamoglu, “Giant paramagnetism-induced valley polarization of electrons in charge-tunable monolayer MoSe_2 ,” *Physical Review Letters* **118**, 237404 (2017).
- [31] Jonas Gaël Roch, Guillaume Froehlicher, Nadine Leisgang, Peter Makk, Kenji Watanabe, Takashi Taniguchi, and Richard John Warburton, “Spin-polarized electrons in monolayer MoS_2 ,” *Nature Nanotechnology* **14**, 432–436 (2019).
- [32] Erfu Liu, Jeremiah van Baren, Zhengguang Lu, Takashi Taniguchi, Kenji Watanabe, Dmitry Smirnov, Yia-Chung Chang, and Chun Hung Lui, “Exciton-polaron Rydberg states in monolayer MoSe_2 and WSe_2 ,” *Nature Communications* **12** (2021).
- [33] You Zhou, Jiho Sung, Elise Brutschea, Ilya Esterlis, Yao Wang, Giovanni Scuri, Ryan J Gelly, Hoseok Heo, Takashi Taniguchi, Kenji Watanabe, *et al.*, “Bilayer Wigner crystals in a transition metal dichalcogenide heterostructure,” *Nature* **595**, 48–52 (2021).
- [34] Hema CP Movva, Timothy Lovorn, Babak Fallahazad, Stefano Larentis, Kyoungwan Kim, Takashi Taniguchi, Kenji Watanabe, Sanjay K Banerjee, Allan H MacDonald, and Emanuel Tutuc, “Tunable Γ -K Valley Populations in Hole-Doped Trilayer WSe_2 ,” *Physical Review Letters* **120**, 107703 (2018).
- [35] Chenhao Jin, Emma C Regan, Aiming Yan, M Iqbal Bakti Utama, Danqing Wang, Sihan Zhao, Ying Qin, Sijie Yang, Zhiren Zheng, Shenyang Shi, *et al.*, “Observation of moiré excitons in WSe_2/WS_2 heterostructure superlattices,” *Nature* **567**, 76–80 (2019).
- [36] David A Ruiz-Tijerina and Vladimir I Fal’ko, “Interlayer hybridization and moiré superlattice minibands for electrons and excitons in heterobilayers of transition-metal dichalcogenides,” *Physical Review B* **99**, 125424 (2019).
- [37] Aaron M Jones, Hongyi Yu, Jason S Ross, Philip Klement, Nirmal J Ghimire, Jiaqiang Yan, David G Mandrus, Wang Yao, and Xiaodong Xu, “Spin-layer locking effects in optical orientation of exciton spin in bilayer WSe_2 ,” *Nature Physics* **10**, 130–134 (2014).
- [38] Mauro Brotons-Gisbert, Hyeonjun Baek, Alejandro Molina-Sánchez, Aidan Campbell, Eleanor Scerri, Daniel White, Kenji Watanabe, Takashi Taniguchi, Cristian Bonato, and Brian D Gerardot, “Spin-layer locking of interlayer excitons trapped in moiré potentials,” *Nature Materials* **19**, 630–636 (2020).
- [39] E Courtade, M Semina, M Manca, MM Glazov, Cédric Robert, F Cadiz, G Wang, T Taniguchi, K Watanabe, M Pierre, *et al.*, “Charged excitons in monolayer WSe_2 : experiment and theory,” *Physical Review B* **96**, 085302 (2017).
- [40] Zefang Wang, Yi-Hsin Chiu, Kevin Honz, Kin Fai Mak, and Jie Shan, “Electrical tuning of interlayer exciton gases in WSe_2 bilayers,” *Nano Letters* **18**, 137–143 (2018).
- [41] Mit H Naik, Emma C Regan, Zuocheng Zhang, Yang-Hao Chan, Zhenglu Li, Danqing Wang, Yoseob Yoon, Chin Shen Ong, Wenyu Zhao, Sihan Zhao, *et al.*, “Intralayer charge-transfer moiré excitons in van der Waals superlattices,” *Nature* **609**, 52–57 (2022).
- [42] Erfu Liu, Jeremiah van Baren, Takashi Taniguchi, Kenji Watanabe, Yia-Chung Chang, and Chun Hung Lui, “Landau-quantized excitonic absorption and luminescence in a monolayer valley semiconductor,” *Physical Review Letters* **124**, 097401 (2020).
- [43] Tianmeng Wang, Zhipeng Li, Zhengguang Lu, Yunmei Li, Shengnan Miao, Zhen Lian, Yuze Meng, Mark Blei, Takashi Taniguchi, Kenji Watanabe, *et al.*, “Observation of Quantized Exciton Energies in Monolayer WSe_2 under a Strong Magnetic Field,” *Physical Review X* **10**, 021024 (2020).
- [44] Ajit Srivastava, Meinrad Sidler, Adrien V Allain, Dominik S Lembke, Andras Kis, and Atac Imamoglu, “Valley Zeeman effect in elementary optical excitations of monolayer WSe_2 ,” *Nature Physics* **11**, 141–147 (2015).
- [45] Jonathan Förste, Nikita V Tepliakov, Stanislav Yu Kruchinin, Jessica Lindlau, Victor Funk, Michael Förg, Kenji Watanabe, Takashi Taniguchi, Anvar S Baimuratov, and Alexander Högele, “Exciton g-factors in monolayer and bilayer WSe_2 from experiment and theory,” *Nature Communications* **11**, 4539 (2020).
- [46] Kevin Slagle and Liang Fu, “Charge transfer excitations, pair density waves, and superconductivity in moiré materials,” *Physical Review B* **102**, 235423 (2020).
- [47] Amir Dalal and Jonathan Ruhman, “Orbitally selective Mott phase in electron-doped twisted transition metal dichalcogenides: A possible realization of the Kondo lattice model,” *Physical Review Research* **3**, 043173 (2021).

- [48] Ajesh Kumar, Nai Chao Hu, Allan H MacDonald, and Andrew C Potter, “Gate-tunable heavy fermion quantum criticality in a moiré Kondo lattice,” *Physical Review B* **106**, L041116 (2022).
- [49] Archana Raja, Andrey Chaves, Jaeun Yu, Ghidewon Arefe, Heather M Hill, Albert F Rigosi, Timothy C Berkelbach, Philipp Nagler, Christian Schüller, Tobias Korn, *et al.*, “Coulomb engineering of the bandgap and excitons in two-dimensional materials,” *Nature Communications* **8**, 15251 (2017).
- [50] Dongxue Chen, Zhen Lian, Xiong Huang, Ying Su, Mina Rashetnia, Lei Ma, Li Yan, Mark Blei, Li Xiang, Takashi Taniguchi, *et al.*, “Excitonic insulator in a heterojunction moiré superlattice,” *Nature Physics* **18**, 1171–1176 (2022).
- [51] Meinrad Sidler, Patrick Back, Ovidiu Cotlet, Ajit Srivastava, Thomas Fink, Martin Kroner, Eugene Demler, and Atac Imamoglu, “Fermi polaron-polaritons in charge-tunable atomically thin semiconductors,” *Nature Physics* **13**, 255–261 (2017).
- [52] Dmitry K Efimkin and Allan H MacDonald, “Many-body theory of trion absorption features in two-dimensional semiconductors,” *Physical Review B* **95**, 035417 (2017).
- [53] Christian Fey, Peter Schmelcher, Atac Imamoglu, and Richard Schmidt, “Theory of exciton-electron scattering in atomically thin semiconductors,” *Physical Review B* **101**, 195417 (2020).
- [54] Zefang Wang, Liang Zhao, Kin Fai Mak, and Jie Shan, “Probing the spin-polarized electronic band structure in monolayer transition metal dichalcogenides by optical spectroscopy,” *Nano letters* **17**, 740–746 (2017).
- [55] Shiyuan Gao, Yufeng Liang, Catalin D Spataru, and Li Yang, “Dynamical excitonic effects in doped two-dimensional semiconductors,” *Nano Letters* **16**, 5568–5573 (2016).
- [56] Kaiyuan Yao, Aiming Yan, Salman Kahn, Aslihan Suslu, Yufeng Liang, Edward S Barnard, Sefaattin Tongay, Alex Zettl, Nicholas J Borys, and P James Schuck, “Optically discriminating carrier-induced quasiparticle band gap and exciton energy renormalization in monolayer MoS₂,” *Physical Review Letters* **119**, 087401 (2017).
- [57] Luis A Jauregui, Andrew Y Joe, Kateryna Pistunova, Dominik S Wild, Alexander A High, You Zhou, Giovanni Scuri, Kristiaan De Greve, Andrey Sushko, Che-Hang Yu, *et al.*, “Electrical control of interlayer exciton dynamics in atomically thin heterostructures,” *Science* **366**, 870–875 (2019).
- [58] Lothar H Brixner, “Preparation and properties of the single crystalline ab₂-type selenides and tellurides of niobium, tantalum, molybdenum and tungsten,” *Journal of Inorganic and Nuclear Chemistry* **24**, 257–263 (1962).
- [59] Akash Laturia, Maarten L Van de Put, and William G Vandenberghe, “Dielectric properties of hexagonal boron nitride and transition metal dichalcogenides: from monolayer to bulk,” *npj 2D Materials and Applications* **2** (2018).
- [60] H Baek, M Brotons-Gisbert, ZX Koong, A Campbell, M Rambach, K Watanabe, T Taniguchi, and BD Gerardot, “Highly energy-tunable quantum light from moiré-trapped excitons,” *Science Advances* **6**, eaba8526 (2020).
- [61] Mauro Brotons-Gisbert, Hyeonjun Baek, Aidan Campbell, Kenji Watanabe, Takashi Taniguchi, and Brian D Gerardot, “Moiré-trapped interlayer trions in a charge-tunable WSe₂/MoSe₂ heterobilayer,” *Physical Review X* **11**, 031033 (2021).
- [62] A. P. Thompson, H. M. Aktulga, R. Berger, D. S. Bolintineanu, W. M. Brown, P. S. Crozier, P. J. in ’t Veld, A. Kohlmeyer, S. G. Moore, T. D. Nguyen, R. Shan, M. J. Stevens, J. Tranchida, C. Trott, and S. J. Plimpton, “LAMMPS - a flexible simulation tool for particle-based materials modeling at the atomic, meso, and continuum scales,” *Comp. Phys. Comm.* **271**, 108171 (2022).
- [63] José M Soler, Emilio Artacho, Julian D Gale, Alberto García, Javier Junquera, Pablo Ordejón, and Daniel Sánchez-Portal, “The siesta method for ab initio order-n materials simulation,” *Journal of Physics: Condensed Matter* **14**, 2745 (2002).
- [64] W. Kohn and L. J. Sham, “Self-consistent equations including exchange and correlation effects,” *Phys. Rev.* **140**, A1133–A1138 (1965).
- [65] L Fernández-Seivane, M A Oliveira, S Sanvito, and J Ferrer, “On-site approximation for spin-orbit coupling in linear combination of atomic orbitals density functional methods,” *Journal of Physics: Condensed Matter* **18**, 7999 (2006).
- [66] N. Troullier and José Luís Martins, “Efficient pseudopotentials for plane-wave calculations,” *Phys. Rev. B* **43**, 1993–2006 (1991).
- [67] Nick Papior, Nicolás Lorente, Thomas Frederiksen, Alberto García, and Mads Brandbyge, “Improvements on non-equilibrium and transport green function techniques: The next-generation transiesta,” *Computer Physics Communications* **212**, 8–24 (2017).

DATA AVAILABILITY

The datasets generated and analysed during the current study are available from the corresponding author on reasonable request.

ACKNOWLEDGEMENTS

We thank Jonathan Ruhman for insightful discussions. This work was supported by the EPSRC (grant nos. EP/P029892/1 and EP/L015110/1), and the ERC (grant no. 725920). V.V and J.L. acknowledge funding from the EPSRC (grant no. EP/S025324/1). This work used the ARCHER2 UK National Supercomputing Service via J.L.’s membership of the HEC Materials Chemistry Consortium of UK, which is funded by EPSRC (EP/L000202). This project has received funding from the European Union’s Horizon 2020 research and innovation programme under the Marie Skłodowska-Curie grant agreement No. 101067977. M.B.-G. is supported by a Royal Society University Research Fellowship. B.D.G. is supported by a Wolfson Merit Award from the Royal Society and a Chair in Emerging Technology from the Royal Academy of Engineering. K.W. and T.T. acknowledge support from the Elemental Strategy Initiative conducted by the MEXT, Japan, grant no. JP-MXP0112101001, JSPS KAKENHI grant no. 19H05790

and JP20H00354.

CONTRIBUTIONS

A.C. performed the experimental measurements. A.C., M.B.G., and B.D.G. analysed the data. H.B. fabricated the sample. V.V. and J.L. performed the theoretical calculations. T.T. and J.W. grew the hBN crystals. B.D.G. and J.L. conceived and supervised the project. A.C., V.V., M.B.G, J.L. and B.D.G. and wrote the manuscript with input from all authors.